

A Viscous Vorticity Method for Propeller Tip Flows and Leading Edge Vortex

Ye Tian¹, Spyros A. Kinnas²

^{1,2} Ocean Engineering Group, Department of Civil, Architectural and Environmental Engineering
The University of Texas at Austin, Austin, TX 78712, USA

ABSTRACT

A novel numerical method solves the VIScous Vorticity Equation (VISVE) in 3D is presented in this paper. The method was proposed by Tian and Kinnas (2014) in order to model the Leading Edge Vortex (LEV) and Tip Vortex (TV) of propellers. The spatial concentration of the vorticity is exploited in the method, which is designed to be spatially compact and numerically efficient, in the meantime, capable of modeling complicated vorticity/solid boundary interaction in 2D and 3D.

In this paper, the VISVE method is improved by including a potential wake model in order to handle the flow in far downstream. A block-structured gridding strategy suitable for round tip propellers is also introduced. The method is validated in the case of a 2D hydrofoil at high angle of attack against the results from Navier-Stokes (NS) simulation. The method is then applied in the cases of two single bladed propellers, one has a squared tip and another has a round tip. In the end, the method is used to simulate a real five bladed propeller at very low advance ratio.

Keywords

Leading Edge Vortex; Propeller Tip Flows; Vorticity Method

1 INTRODUCTION

Modeling the propeller tip flows and the leading edge vortex can be challenging for potential flow methods. Propeller LEVs and TVs are often spatially distributed vortical flow structures that are difficult to be represented using line and panel singularities which are fundamental in potential flow methods. In addition, strong vorticity and wall boundary interaction creates more numerical troubles, since in the vicinity of wall boundaries the induced velocity due to the representing singularities of the blade is not smooth. Improper modeling of the LEVs and TVs can easily lead to crash of simulations.

In the meantime, a numerical model for propeller tip flows and LEVs is necessary, if the off-design performance is of interest. At high loading, the LEV passes over the

propeller blade and significantly changes the load distribution. On moderately high loading conditions, the LEV also alters the flow patterns near the tip of the propeller blade. Without a LEV model, panel methods are set to under-predict the thrust and torque of propellers at high loading.

The success of the simulating the unsteady trailing edge wake in 2D through vortex tracing attracted many researchers to study the leading edge separated flows with the same method. Katz (1981) applied a discrete vortex method to an airfoil at high angle of attack in order to study the post-stall aerodynamic behavior of the airfoil. The foil was modeled through a 2D vortex lattice approach, and the Kutta conditions were imposed at both the trailing edge and also the separation point. Katz suggested that the methods could be applied to foils with round leading edge by multiplying a circulation reduction factor on the shed vortex strength. The numerical results were largely in a good agreement with the experimental data on lifts and drags. The LEV model was turned on and off manually according to the experimental data. At moderate high angle of attack ($14\text{DEG} < \text{AOA} < 20 \text{ DEG}$), the separation point was also chosen to fit the experimental observation. Spalart and Leonard (1981) presented a more general vortex tracking approach for separated flows. This approach gave up the thin shear layer assumption on the LEV. All the vortices created on the solid surface were allowed to enter the fluid domain. The discrete vortices were traced individually in time, and these vortices form “vorticity cloud” in the fluid domain. Large Reynolds number assumption was presumed, and boundary layer calculation was necessary to create the Reynolds number dependency of the results. The vortex method by Spalart and Leonard (1981) was developed continuously by the second author later on. Koumoutsakos and Leonard (1995) applied the improved vortex method to an impulsively started cylinder with high-resolution over a wide range of Reynolds numbers ($\text{Re}=40$ to 9500). The viscosity in the improved method was treated more rigorously so that the boundary layer calculation was no long necessary.

In the 1970s and 1980s, the aerodynamic community devoted great effort to analyzing the delta wings with sharp leading edge at high angle of attack. Kandil et al. (1976) proposed a Vortex Lattice Method for wings with LEV. The LEV geometry was represented by a horseshoe vortex system similar to that of the tailing edge wake. An iterative alignment procedure was applied to adjust the vortex segments in the same direction of the local flow velocity. Gordon and Rom (1985) presented a similar approach for the delta wing with a different arrangement of the surface singularities. Both methods lead to good correlation with experimental measurements on global forces such as the lift and pitching moment. Yet the correlations on pressure distributions were not emphasized. At the same time, a team in the Boeing Company invented a different approach to treat the LEV and also the wake system for wings. The methods were summarized by Johnson et al. (1980). In their methods, the free LEV/wake sheets were treated as no penetration surfaces. A few geometric parameters, such as the panel length and roll-up angle were used to describe the LEV and the rolling up part of the wake sheets.

However, these methods for delta wings with sharp leading edge more or less suffer from numerical difficulties at low to moderate angle of attack. The smoothness of the induced velocities due to the wing start to deteriorate as the LEV sheet approaches close to the wing. At the same time, the LEV induced velocities on the wing could also be inaccurate. A numerical fence is usually necessary to keep the code from crashing.

An early study on propeller tip flow was conducted by Greeley (1982), who essentially treated the LEV with a combination of empirical and numerical methods. Later, Lee et al (2002, 2004) developed a 3-D wake model based on low order panel method for marine propeller, which is able to predict developed tip vortex cavity. The tip vortex cavity is modeled with a cylindrical vortex tube. L. He (2010) extended Lee's wake model in order to be able to take some viscous effects into account. In He's study, different viscous core was tested. All these studies treated the propeller wake as a distinct shear layer and gained success. Intuitively, efforts were made to apply the distinct shear layer model for the wake to the LEV as well. Singh and Kinnas (2009) applied He's algorithm to 2D hydrofoils with LEV separation, and obtained some preliminary results. Tian and Kinnas (2011) implemented the 3D distinct shear layer model for the LEV for delta wings with sharp leading edge and also propeller blades. Although their investigation produced meaningful results, the correlation with RANS indicated that certain numerical and physical defects in the distinct shear layer model created difficulties to correctly simulate the LEV. Two major problems were: 1) there was no easy way to determine the detachment point of the LEV; 2) it was impossible to handle the viscous interaction between the LEV and wall boundaries. In order to overcome these difficulties, Tian and Kinnas (2014) proposed a vortical flow model which locally solves the VIScous Vorticity Equation (VISVE). More details of the

method can be found in the PH.D dissertation by Tian (2014).

The VISVE model for the LEV takes the advantage of the fact that the vorticity in the flow field concentrate in a small region close to the wall boundary. Therefore the computational domain for solving the vorticity equation is significantly reduced. A low order panel method code (PROPCAV) is adopted to provide the appropriate boundary condition on the wall. Correspondingly the spatial grid for the vorticity equation is conformal to the boundary grid in the panel method. The LEV model finally can work as a local correction to the inviscid solutions from the panel method.

In Tian and Kinnas (2014), the VISVE method was only used to model the impulsive starting of propellers since there was no wake model included. In this paper, a potential wake model enables the method to be able to reach steady solutions. Moreover, the gridding strategy is also improved to create highly orthogonal mesh around the propeller tip for propellers having round tips. The progresses made in the development the VISVE method are summarized in this paper.

2 FORMULATION

2.1 Velocity Decomposition

In order to use an existing panel method, the velocity field \mathbf{q} is decomposed as follows:

$$\mathbf{q} = \mathbf{U}_\infty + \nabla\phi + \mathbf{u}_\omega \quad (1)$$

where \mathbf{q} is the total velocity, \mathbf{U}_∞ is the inflow velocity, $\nabla\phi$ is the potential velocity, and \mathbf{u}_ω is the rotational velocity, where $\nabla \times \mathbf{u}_\omega = \boldsymbol{\omega}$; $\boldsymbol{\omega}$ represents the vorticity. To make the decomposition unique \mathbf{u}_ω is the free space induced velocity due to $\boldsymbol{\omega}$.

2.2 Viscous Vorticity Equation

The Viscous Vorticity Equation (VISVE) is written as:

$$\frac{\partial \boldsymbol{\omega}}{\partial t} + \nabla \times (\boldsymbol{\omega} \times \mathbf{q}) = -\nu \nabla \times (\nabla \times \boldsymbol{\omega}) \quad (2)$$

where ν is the kinematic viscosity of the fluid. Clearly (2) is not in the often conservative form description of the vorticity equation but is in the 'curl form', which can enforce the solenoidal vorticity field. Theoretically, for a given vorticity field $\boldsymbol{\omega}$ if one can calculate the corresponding velocity field \mathbf{q} which satisfies both the continuity equation and the boundary conditions, one can march (2) to the next time level and thus evolve the vorticity field.

A special staggered arrangement is used to solve (2). As shown in Figure 1, the face projection of vorticity is located at the centroid of a face ($\omega_i = \boldsymbol{\omega} \cdot \mathbf{n}_i, i = 1, 2, 3$) and velocity vectors are stored in the center of the surrounding edges of a face. The numbers in the parenthesis indicate the local index of a location. For getting the global index, a (i, j, k) triplet has to be added on top of the local index. For example, the global index for $(1, \frac{1}{2}, 0)$ is $(i+1, j+\frac{1}{2}, k)$.

Apparently it is convenient to apply the Stokes' theorem with the staggered arrangement. For example, for ω_2 on face $(\frac{1}{2}, 1, \frac{1}{2})$, we have

$$(A_2 \omega_2)_{\frac{1}{2}, 1, \frac{1}{2}} = (\mathbf{q} \cdot \Delta \mathbf{l}_3)_{0, 1, \frac{1}{2}} - (\mathbf{q} \cdot \Delta \mathbf{l}_3)_{1, 1, \frac{1}{2}} + (\mathbf{q} \cdot \Delta \mathbf{l}_1)_{\frac{1}{2}, 1, 0} - (\mathbf{q} \cdot \Delta \mathbf{l}_1)_{\frac{1}{2}, 1, 1} \quad (3)$$

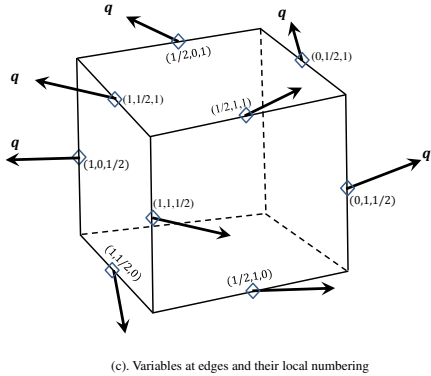
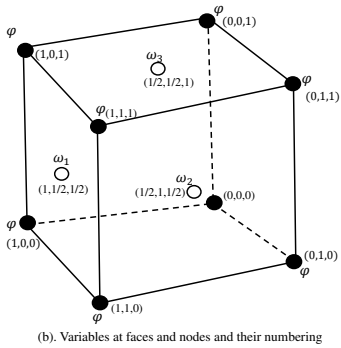
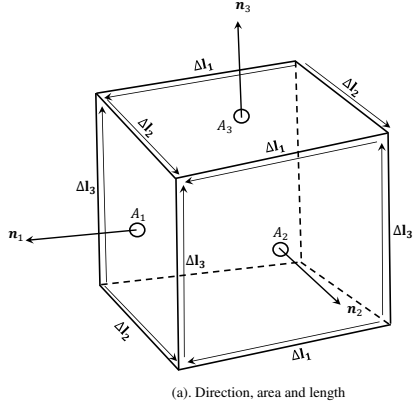


Figure 1: Staggered arrangement of variables.

With the staggered arrangement, the curl operators in (2) can be easily discretized:

$$A \frac{\partial \boldsymbol{\omega} \cdot \mathbf{n}}{\partial t} + \sum_{\partial A} (\boldsymbol{\omega} \times \mathbf{q}) \cdot \Delta \mathbf{l} = -\nu \sum_{\partial A} (\nabla \times \boldsymbol{\omega}) \cdot \Delta \mathbf{l} \quad (4)$$

where A is the face area, \mathbf{n} is the face normal. Further discretization of the second term in the LHS and the RHS term in (4) is discussed in great detail in Tian (2014).

Consider marching from time level n to $n+1$, we know \mathbf{q}^n and $\boldsymbol{\omega}^n$ and want to find $\boldsymbol{\omega}^{n+1}$, backward Euler scheme is adopted to discrete (4) in time.

$$A_i \frac{\omega_i^{n+1} - \omega_i^n}{\Delta t} + \sum_{\partial A} (\boldsymbol{\omega}^{n+1} \times \mathbf{q}^n) \cdot \Delta \mathbf{l} = -\nu \sum_{\partial A} (\nabla \times \boldsymbol{\omega}^{n+1}) \cdot \Delta \mathbf{l} \quad (5)$$

It is worth noting that (5) is not strictly backward Euler scheme since the sup-script of \mathbf{q} is n but not $n+1$. One may iterate (5) by updating \mathbf{q} once $\boldsymbol{\omega}^{n+1}$ is known.

2.3 Vorticity-Velocity Solver

Since the velocity field is required in order to solve (5), a vorticity-velocity solver that determines the velocity field from a given vorticity field is essential in our method.

For calculating the velocity field, the most straightforward way is to directly integrate the vorticity field with a Biot-Savart kernel. A more feasible approach is via a stream function ψ :

$$\psi = -\frac{1}{4\pi} \iiint_V \frac{\boldsymbol{\omega}}{r} dV \quad (6)$$

$$\mathbf{u}_\omega = \nabla \times \psi \quad (7)$$

(6) and (7) can be used to specify the boundary conditions. However, direct integration using (6) and (7) at all the computational points is expensive, since the computational cost is proportional to N^2 where N is the number of unknowns.

Alternatively we can consider computing the velocity field via a Poisson solver. A common technique is to take the curl of (7):

$$\nabla \times (\nabla \times \psi) = \boldsymbol{\omega} \quad (8)$$

which leads to

$$-\nabla^2 \psi = \boldsymbol{\omega} \quad (9)$$

if and only if

$$\nabla \cdot \psi = 0 \quad (10)$$

Eqn. (9) and (10) are convenient to implement in 2D, in which case the streamfunction ψ becomes a scalar and (10) is automatically satisfied. However, in 3D, (9) become three Poisson equations and (10) is even more difficult to enforce in a discretized sense. A more efficient way in 3D is to use a projection method similar to those for solving the Navier-Stokes equation (e.g. Chorin 1967).

Consider an approximation of the velocity field which preserves the vorticity field:

$$\nabla \times \tilde{\mathbf{u}}_\omega = \boldsymbol{\omega} \quad (11)$$

$\tilde{\mathbf{u}}_\omega$ does not necessarily satisfy the continuity equation. We can add a potential correction on top of $\tilde{\mathbf{u}}_\omega$, or in CFD terminology project $\tilde{\mathbf{u}}_\omega$ onto an irrotational flow field $\nabla \varphi$, to enforce the continuity equation:

$$\mathbf{u}_\omega = \tilde{\mathbf{u}}_\omega + \nabla \varphi \quad (12)$$

Take the divergence of (9), we have:

$$\nabla^2 \varphi = -\nabla \cdot \tilde{\mathbf{u}}_\omega \quad (13)$$

The construction of $\tilde{\mathbf{u}}_\omega$ is closely related to (5). It can be easily shown that the follow construction:

$$\tilde{\mathbf{u}}_\omega^{n+1} = \Delta t \mathbf{q}^n \times \boldsymbol{\omega}^{n+1} - \nu \Delta t \nabla \times \boldsymbol{\omega}^{n+1} + \mathbf{u}_\omega^n \quad (14)$$

$$\nabla^2 \varphi = -\nabla \cdot \tilde{\mathbf{u}}_\omega^{n+1} \quad (15)$$

$$\mathbf{u}_\omega^{n+1} = \tilde{\mathbf{u}}_\omega^{n+1} + \nabla \varphi \quad (16)$$

are consistent with (5). It is worth noting that (14) is explicit, because once (5) is solved, the RHS of (14) are all known.

The Poisson equation (15) can be solved using the standard Finite Volume Method (FVM). On the far-field boundary, (6) and (7) are adopted to provide a Neumann boundary condition. On the wall a Neumann boundary condition can also be obtained by eliminating the normal velocity.

2.4 Vorticity Creation on the Wall

On the wall both normal velocity and tangential velocity have to be eliminated. However the Poisson solver (15) cannot enforce both no-slip and no-penetrating boundary conditions. A vorticity creation algorithm is crucial to diminish both the normal velocity and the slip velocity.

Consider solving (5) without having new vorticity generated on the wall, we have a vorticity field $\boldsymbol{\omega}^{n+1*}$, which induces a normal velocity on the wall. The normal velocity can be excluded using boundary element methods which give a surface vorticity distribution γ on the wall. Koumoutsakos and Leonard (1995) reasoned that γ can be translated to a vorticity flux:

$$\nu \frac{\partial \boldsymbol{\omega}^{n+1**}}{\partial n} = \frac{\gamma(\boldsymbol{\omega}^{n+1*})}{\Delta t} \quad (17)$$

The $\boldsymbol{\omega}^{n+1**}$ is the correction of $\boldsymbol{\omega}^{n+1*}$ and enters the flow field via viscous diffusion:

$$A_i \frac{\omega_i^{n+1**}}{\Delta t} = -\nu \sum_{\partial A} (\nabla \times \boldsymbol{\omega}^{n+1**}) \cdot \Delta l \quad (18)$$

$$\boldsymbol{\omega}^{n+1} = \boldsymbol{\omega}^{n+1*} + \boldsymbol{\omega}^{n+1**} \quad (19)$$

In the present method, (17)-(19) are adopted. Numerical results show that (17)-(19) approximate the no-slip boundary reasonably well. However, an $O(\Delta t)$ error exists in (18) since a $\boldsymbol{\omega}^{n+1*} \times \mathbf{q}$ term is missing. This first order error unfortunately does not vanish as the solution approaches the steady state. Elimination of the mentioned error must be addressed in the future.

2.5 Potential Wake Model

The wake of a propeller extends for a considerably long distance. In order to retain the spatial compactness of the method, a potential wake model, which works well for boundary element method, is included.

As shown in Figure 2, the trailing edge wake of a propeller is modeled as three parts: 1). the VISVE wake; 2). the near potential wake; 3). the far potential wake.

The VISVE wake is the natural extension of the computational domain after the tailing edge of the propeller blade. In this region, the VISVE is still solved. The total vorticity across the end of the VISVE wake, denoted as Γ_W , are passed to the near potential wake.

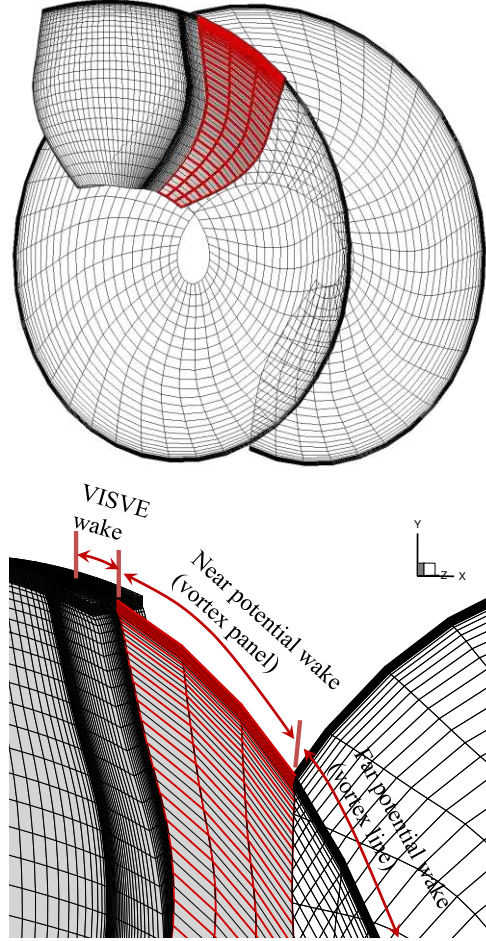


Figure 2: Schematic plot of the wake model for a propeller.

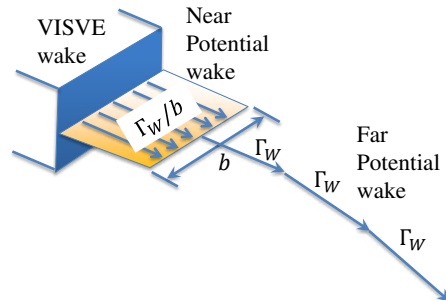


Figure 3: Strength of the singularities on the potential wake.

As shown in Figure 3, in the near potential wake region, the wake is modeled using constant vortex panels. The strength of the vortex equals to Γ_W , where b is the width of the panel.

In the far potential wake region, the wake is modeled using vortex lines. The vortex strength for each line is specified as Γ_W .

2.6 Rotational Frame of Reference

When modeling the propeller flow, it is convenient to use the rotational frame of reference. In the meantime, the background rotation carries a uniform vorticity, which must be excluded from the vorticity field when solving the VISVE.

For a right handed propeller operating with rotational speed Ω , the rotational velocity vector is $(-\Omega, 0, 0)$. Denoting $\Omega = (\Omega, 0, 0)$, we have

$$\mathbf{q}_r = \mathbf{q}_a + \boldsymbol{\Omega} \times \mathbf{r} \quad (20)$$

where \mathbf{q}_a is the velocity under the inertial frame of reference, and \mathbf{q}_r is the velocity in the rotational frame of reference. $\mathbf{r} = (0, y, z)$ is the radial vector of a field point. The vorticity $\boldsymbol{\omega}$ is defined under the inertial frame of reference:

$$\boldsymbol{\omega} = \nabla \times \mathbf{q}_a \quad (21)$$

The background rotation add a constant vorticity 2Ω into the relative velocity field \mathbf{q}_r :

$$\boldsymbol{\omega} + 2\boldsymbol{\Omega} = \nabla \times \mathbf{q}_r \quad (22)$$

With some manipulation, the momentum equation can be written as:

$$\begin{aligned} \frac{\partial \mathbf{q}_r}{\partial t} + \nabla \left(\frac{q_r^2}{2} + P - \frac{\Omega^2 r^2}{2} \right) \\ = \mathbf{q}_r \times \boldsymbol{\omega} - \nu(\nabla \times \boldsymbol{\omega}) \end{aligned} \quad (23)$$

Taking the curl of (23) leads to the VISVE in the rotational frame of reference:

$$\frac{\partial \boldsymbol{\omega}}{\partial t} + \nabla \times (\boldsymbol{\omega} \times \mathbf{q}_r) = -\nu \nabla \times (\nabla \times \boldsymbol{\omega}) \quad (24)$$

(24) shows that in the rotational frame of reference, the VISVE keeps the same form as in the inertial frame of reference.

2.7 Pressure Calculation

In the VISVE, pressure is not a primitive variable and has to be calculated through post-processing. Define the total head H as:

$$H = \frac{q_r^2}{2} + P - \frac{\Omega^2 r^2}{2} \quad (25)$$

From (21) we can obtain:

$$\nabla H = -\frac{\partial \mathbf{q}_r}{\partial t} + \mathbf{q}_r \times \boldsymbol{\omega} - \nu(\nabla \times \boldsymbol{\omega}) \quad (26)$$

Integrating the RHS of (25) gives H , and consequently, the pressure P .

2.7 Grid Generation

In (Tian and Kinnas 2014) the VISVE mesh was generated by sweeping a 2D sectional grid in the spanwise direction. This gridding strategy is suitable for impeller blades having squared tip, as shown in Fig. 4. However, for open propellers with a round tip the strategy tends to create

highly skewed cells in the tip region. A block-structured gridding strategy is designed to fit a round tip better, as shown in Fig. 5. Since only the vicinity of the propeller is needed to be modeled, the grid generation process is automated, as an advantage of the VISVE method.

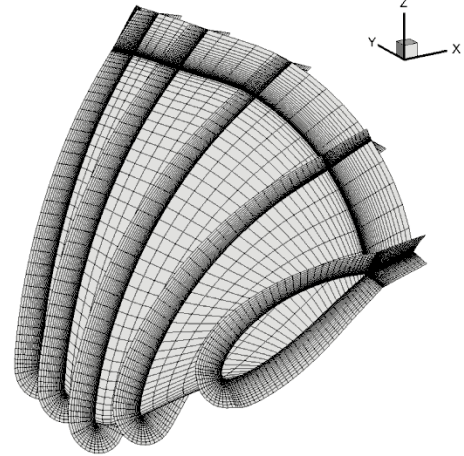


Figure 4: Computational grid for a propeller having a squared tip.

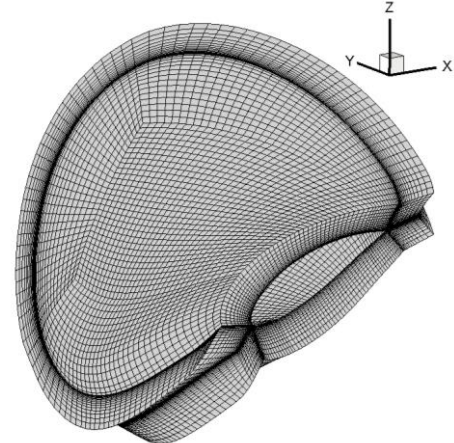


Figure 5: Computational grid for a propeller NSRCD 4381 (Boswell 1871).

2.8 The Effects of Other Blades

Figure 4 and 5 show the computational grid for the key blade, for which the VISVE is solved. The effects of other blades are included by adding their induced velocity into the Neumann boundary condition for the Poisson solver (15). For axisymmetric inflow, the vorticity field around the key blade is simply duplicated when calculating the boundary condition for (15). For non-axisymmetric inflow, the problem can be solved iteratively by assuming that the vorticity field around a certain blade will be the same as the key blade when it is at the same blade angle. This solving technique performs well in our BEM code, PROPCAV. Since the effects of other blades are dealt without using periodic boundary conditions the grid generation process

can be significantly simplified. Making a periodic grid for a low pitch propeller can be extremely difficult even impossible.

3 RESULTS

3.1 A 2D Hydrofoil at High Angle of Attack

The proposed method is first applied in the case of a 2D hydrofoil at 10 degree Angle of Attack (AOA). The Reynolds number is specified to be 5×10^4 . About 7,000 cells are used in the VISVE method. In the meantime, a Navier-Stokes (N-S) simulation performed using ANSYS Fluent, version 14.5, is also carried out in order to validate the results. The N-S simulation uses about 60,000 cells. Fig. 6 compares the computational domains between the two methods.

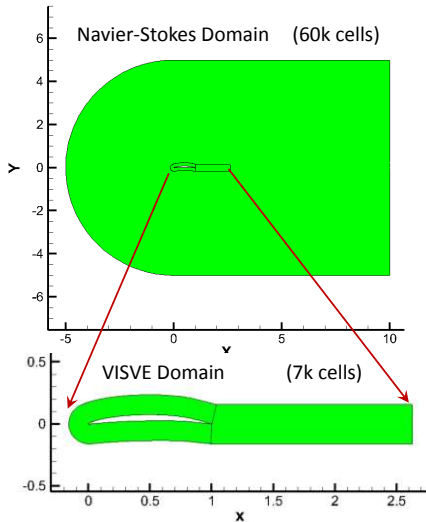


Figure 6: Comparison of the computational domain between N-S and VISVE.

Fig. 7-10 shows the comparison of the predicted vorticity distribution from the VISVE method and the N-S simulation. Reasonable agreement between the two methods can be observed. Particularly the VISVE method is able to predict the secondary vortex due to the strong viscous interaction between the LEV and the wall. Other methods in the inviscid vortex dynamics will fail in this scenario.

3.2 A Single Bladed Propeller with a Squared Tip

The method is then applied in the case of a single bladed propeller with squared tip. As a preliminary test, the propeller only has one blade. The pitch and thickness of the blade are the same as those of a 5 bladed propeller NSRCD 4381 (Boswell 1971). The design advance ratio of NSRCD 4381 is 0.889. Given the fact that single blade propellers have much heavier loading than multi-bladed propellers when both work at the same advance ratio, we consider 0.6 is a low advance ratio for the model propeller.

Fig. 5 shows the computational grid. On the blade 80×25 (chordwise \times spanwise) panels are used, and 20 layers of cells grow in the normal direction.

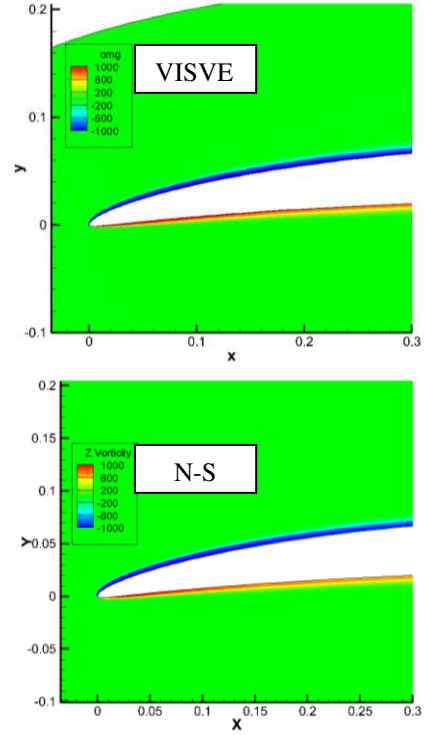


Figure 7: Vorticity distribution at $t=0.5 C/U_\infty$

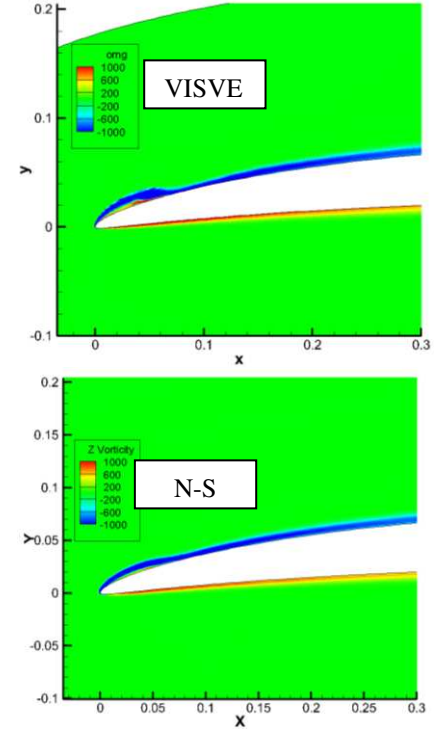


Figure 8: Vorticity distribution at $t=1.0 C/U_\infty$

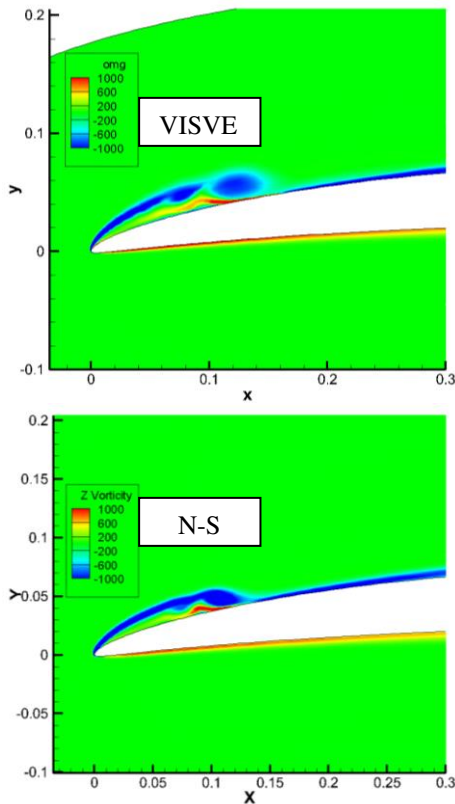


Figure 9: Vorticity distribution at $t=1.5 C/U_\infty$

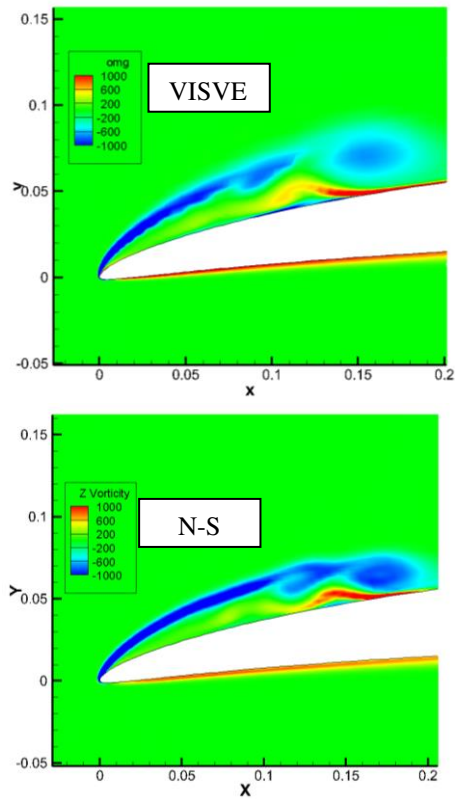


Figure 10: Vorticity distribution at $t=2.0 C/U_\infty$

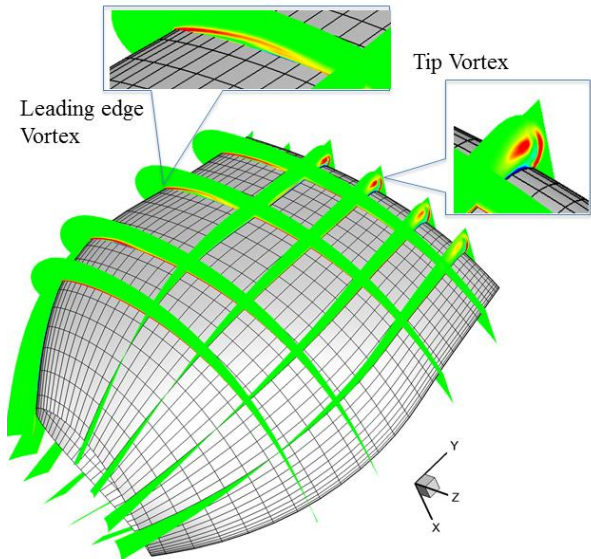


Figure 11: Predicted vorticity distribution around a squared tip propeller at $J=0.6$.

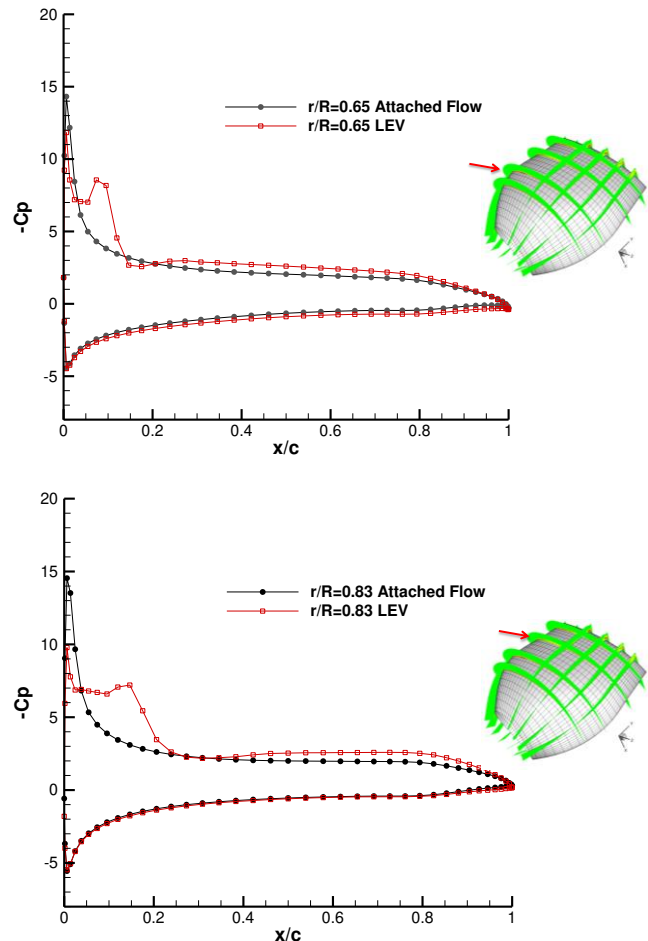


Figure 12: Effect of the LEV on the pressure distribution, $J=0.6$; Top: $r/R=0.65$, Bottom: $r/R=0.83$, $C_p = \frac{P-P_0}{0.5\rho n^2 D^2}$

In the $J = 0.6$ case, the time step size Δt is specified as $0.001[R/U_\infty]$, which is about 10 times of the time step from the CFL condition. Clearly the backward Euler scheme greatly improves the numerical stability of the method. The Reynolds number based on the propeller diameter D and the inflow, $Re_D = 2 \times 10^6$. Fig. 11 shows the predicted vorticity distribution around the propeller. Both the tip vortex and the leading edge vortex are captured by the method. Fig. 12 shows the effect of the LEV on the pressure distribution. As expected, the LEV creates a low pressure plateau close to the leading edge. Conceivably the total torque and thrust with the LEV are increased, as shown in Table 1.

Table 1: Predicted thrust and torque coefficients (KT and KQ) with and without the LEV.

| | Attached Flow | With LEV | Change in % |
|----|---------------|----------|-------------|
| KT | 0.167 | 0.2 | +19% |
| KQ | 0.0289 | 0.0341 | +18% |

The flow around the propeller at an extremely high loading condition: $J=0.3$, is also investigated. In this case the time step size $\Delta t = 0.0005[\frac{R}{U_\infty}]$, because the rotational speed of the propeller is twice of that at $J=0.6$. A slightly bigger computational domain, which has 25 layers of cells in the normal direction, is adopted. Fig. 13 shows the LEV and the tip vortex at the 150th time step from different perspectives. Clearly the LEV becomes more three-dimensional – it has strong components not only in the spanwise cutting sections, but also in the chordwise cutting sections.

3.3 A Single Bladed Propeller with a Round Tip

After improving the gridding strategy for propellers with a round tip, the method can handle more realistic geometry. The propeller NSRCD 4381 is modeled, considering only one blade. The computational grid for this propeller is shown in Fig. 5. The blade surface is represented by 5,100 panels, and 15 layers of cells grow in the normal direction. In total 99,000 cells are used in the simulation. A full-blown RANS simulation for the same propeller with periodic boundaries used about 1.8 million hexahedral cells.

Fig. 14 shows the predicted vorticity field around the propeller blade at $J = 0.889$. Clearly the tip vortices are well captured. Since the advance ratio is just moderately low, the LEV is not heavily formed. Fig. 15 compares the circulation distributions from the VISVE method and BEM. The two circulations are largely in the same shape. In the meantime, the VISVE method predicted more loading than the BEM. It is worth noting that at about $r/R=1$ the circulation from the VISVE method has an inflection point which indicates the tip vortex core as opposed to BEM, which gives an infinite slope of circulation at the tip.

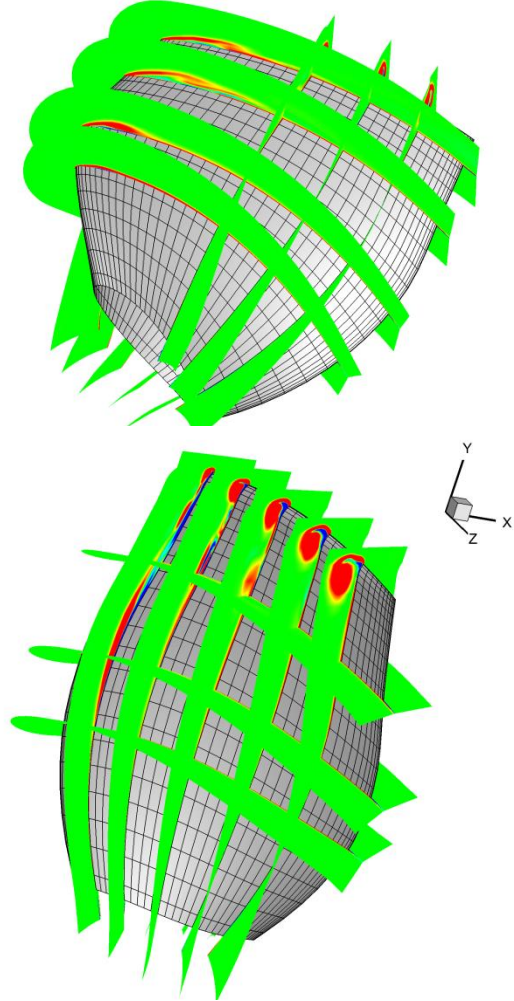


Figure 13: Predicted vorticity distribution around a squared tip propeller at $J=0.3$, $t=0.075[R/U_\infty]$.

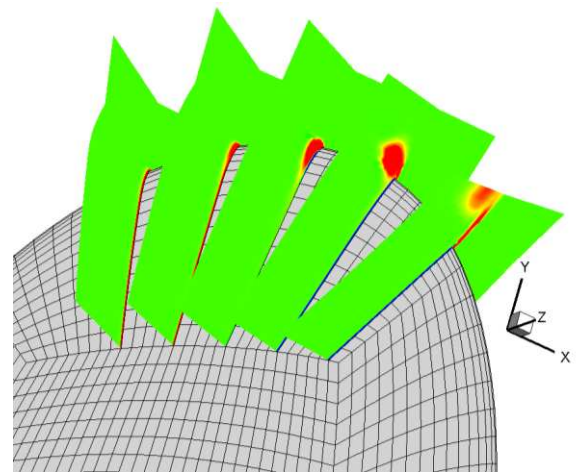


Figure 14: Predicted vorticity distribution around a round tip propeller at $J=0.889$.

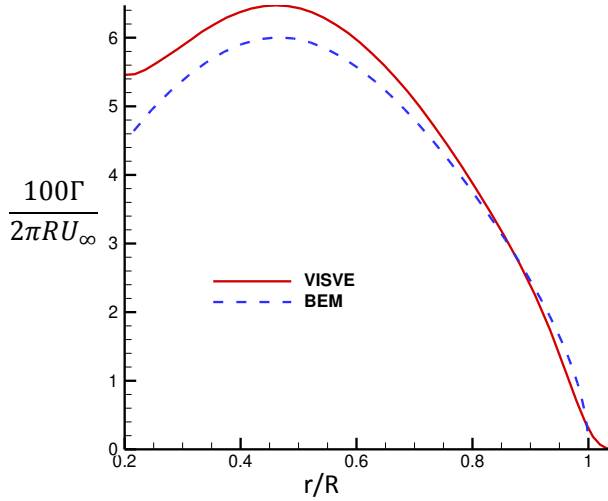


Figure 15: Comparison of circulation distributions between the VISVE method and BEM for a round tip propeller at $J=0.889$.

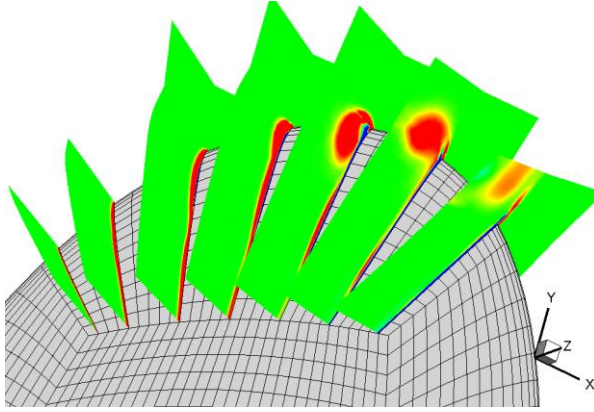


Figure 16: Predicted vorticity distribution around a round tip propeller at $J=0.6$.

Fig. 16 shows the predicted vorticity field around the propeller blade at $J = 0.6$. The tip vortices are more prominent than those at $J = 0.889$. The LEV can also be observed. For round tip propeller, the tip vortex and the LEV are intrinsically the same thing after and before the tip point.

3.4 A Five Bladed Propeller with a Round Tip

Finally the effects of the other 4 blades of the propeller NSRCD 4381 are included. A preliminary test of the method at $J = 0.4$ is carried out. The predicted vorticity distribution looks similar to Fig. 16, as shown in Fig. 17(top). The result from RANS simulation for the same propeller is also plotted in Fig. 17 for comparison. Although it is difficult to show vorticity contours at exactly the same locations, great similarities can be observed between the two results. Fig. 18 shows the predicted circulation from the VISVE method. Clearly a hump close to the tip region

indicates that the presence of the LEV and the tip vortex increase the loading. However, more quantitative correlations have not been made at this stage yet.

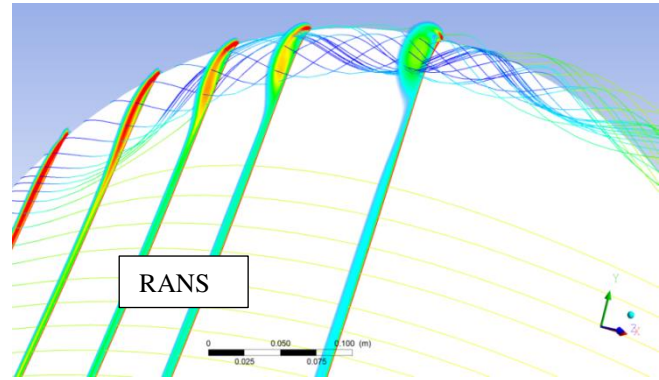
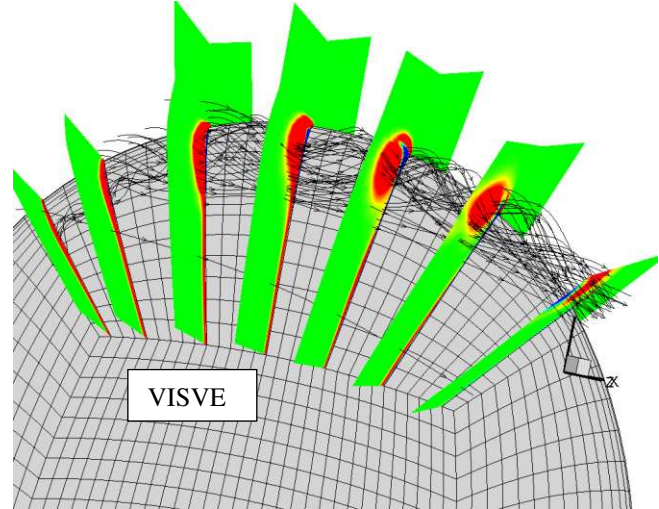


Figure 17: Predicted vorticity distribution around a five bladed round tip propeller (NSRCD 4381) at $J=0.4$ (Top: VISVE, Bottom: RANS).

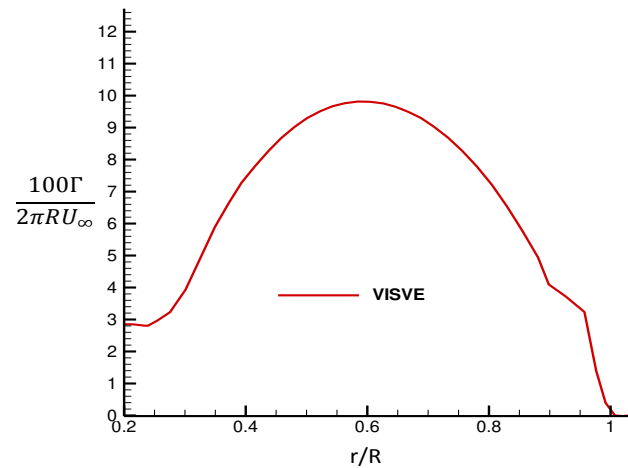


Figure 18: Circulation distribution from the VISVE method for propeller NSRCD 4381 at $J=0.4$.

4 CONCLUSIONS AND FUTURE WORK

In this paper, a numerical method that solves the Viscous Vorticity Equation (VISVE) was presented. The method was implemented in both 2D and 3D in order to model the Leading Edge Vortex (LEV) and tip flows of propeller blades.

The method was first applied in the case of a 2D hydrofoil at high angle of attack. The predicted vorticity distribution was correlated with the result from Navier-Stokes simulation.

The method is then adopted to model the tip flows of both a squared tip propeller and a round tip propeller, using different gridding strategies suitable for each case. Finally the method is used to model a real five bladed propeller at a low advance ratio.

The results for the propeller cases are encouraging. Both the LEV and the tip vortex can be well captured by the method. In the meantime the results for the propeller cases are not correlated with those from other methods or experimental data at the moment. A brief diagnosis indicates that the vorticity creation algorithm may introduce an $O(\Delta t)$ error, which does not diminish as the solutions approach steady state. The present vorticity creation algorithm in the method were particularly designed (by Koumoutsakos,P. and Leonard 1995) for vortex particle methods, which usually use explicit time marching with small Δt , and never seek for steady state solutions.

In the near future, the authors will revisit 2D steady state cases to fully understand the vorticity creation mechanism, and propose a more compatible wall boundary condition. Once the wall boundary condition is improved, the results of the VISVE method will be correlated with those from other methods and available experimental data.

ACKNOWLEDGMENTS

Support for this research was provided by the U.S. Office of Naval Research (Contract No. N00014-07-1-0616, Contract N00014-10-1-0931 and N00014-14-1-0303) and Phases V, VI and VII of the “Consortium on Cavitation Performance of High Speed Propulsors” with the following members: American Bureau of Shipping, Daewoo Shipbuilding and Marine Engineering Co. Ltd., Kawasaki Heavy Industry Ltd., Rolls-Royce Marine AB, Rolls-Royce Marine AS, Samsung Heavy Industries Co. Ltd., SSPA AB, Andritz Hydro GmbH, Wärtsilä Netherlands B.V., Wärtsilä Norway AS, Wärtsilä Lips Defense S.A.S., and Wärtsilä CME Zhenjiang Propeller Co. Ltd., Steerprop Ltd.

REFERENCES

Boswell, R.J. “Design, Cavitation Performance, and Open-Water Performance of a Series of Research – Skewed Propellers”. Report of Naval ship research and development center. Department of the Navy, 1971.

Chorin, A.J., “The numerical solution of the Navier-Stokes equations for an incompressible fluid” Bull. Am. Math. Soc. 73: 928–931, 1967.

Kandil, O.A., Mook, D.T. and Nayfeh, A.H. “Nonlinear Predictions of Aerodynamics Loads on Lifting Surfaces”, Journal of Aircraft, vol 13, 1976

Johnson, F. T. and Lu, P. and Tinoco, E. N. “An improved panel method for the solution of three-dimensional leading-edge vortex flows. Volume 1: Theory document”, NASA-CR-3278, 1980

Katz, J. “A discrete vortex method for the non-steady separated flow over an airfoil”, Journal of Fluid Mechanics, 102:315-328, 1981

Spalart, P. R., and Leonard, A. “Computation of Separated Flows by a Vortex Tracing Algorithm”, AIAA 14th Fluid and Plasma Dynamics Conference, Palo Alto, CA, 1982

Greeley, D. S. and Kerwin, J. E. “Numerical methods for propeller design and analysis in steady flow”. Transactions of Society of Naval Architects&Marine Engineers, 90:415–453., 1982.

Gordon, R. and Rom, J. “Calculation of Non-Linear Subsonic Characteristics of Wings with Thickness and Camber at High Incidence”, AIAA Journal, 23:817-825, 1985

Koumoutsakos,P. and Leonard, A. “High-resolution simulations of the flow around an impulsively started cylinder using vortex methods”, Journal of Fluid Mechanics, 296:1-38., 1995

Lee, H.S. and Kinnas, S. A. “Application of boundary element method in the prediction of unsteady blade sheet and developed tip vortex cavitation on marine propellers”, Journal of Ship Research, 48(1):15-30, 2004

Lee, H.S. “Modeling of unsteady wake alignment and developed tip vortex cavitation”, PH.D dissertation, UT Austin, Aug, 2002.

He, L. “Numerical Simulation of Unsteady Rotor/Stator Interaction and Application to Propeller/Rudder Combination”, PH.D dissertation, UT Austin, Aug, 2010

Singh, S. and Kinnas, S.A. “Prediction of cavitating flow around 3-D straight/swept hydrofoils”, Proceedings of the 7th International Symposium on Cavitation, Ann Arbor, Michigan, USA, August, 2009.

Tian, Y. and Kinnas, S.A. “Modeling of Leading Edge Vortex and its Effects on Propeller Performance”, Second International Symposium on Marine Propulsors (smp'11), Hamburg, Germany, June 2011

Tian, Y. and Kinnas, S.A., "A Vortical Flow Model for the Leading Edge Vortex and Its Effects on Propeller Performance", 30th Symposium on Naval Hydrodynamics, Hobart, Tasmania, Australia, November 2014

Tian, Y. "Leading Edge and Tip Gap Vortex Tracking and its Effect on Propulsor Performance", PH.D dissertation, UT Austin, December, 2014.